Supplementary Material for

4D tomography reveals a complex relationship between wormhole advancement and permeability variation in dissolving rocks

Max P. Cooper[a], Rishabh P. Sharma[a,b], Silvana Magni[a,b], Tomasz P. Blach[c], Andrzej P. Radlinski[c], Katarzyna Drabik[d], Alessandro Tengattini[e,f] and Piotr Szymczak[a]

[a] *Faculty of Physics University of Warsaw Warsaw Poland*

[b] *Institute of Geophysics Polish Academy of Sciences Warsaw Poland*

[c] *University of New South Wales Minerals and Energy Resources Engineering Sydney Australia*

[d] *Oil And Gas Institute - National Research Institute Krakow Poland*

[e] *University Grenoble Alpes CNRS Grenoble INP 3SR 38000 Grenoble France*

[f] *Institute Laue-Langevin 71 avenue des Martyrs - CS 20156 38042 Grenoble Cedex 9 France*

1. Data from Pińczów Experiments

Other dissolution experiments on Pińczów Limestone show the same permeability evolution behaviour to our main experiment, e.g., Figure 1. This example was from a benchtop experiment not subjected to 4D tomography. Flow rate for this experiment was 0.5mL/min, illustrating the permeability evolution behavior is independent of flow rate.

In addition to benchtop experiments, we have performed other dissolution experiments while being scanned with 4D tomography. Figures 2 through 4 show the results from a dissolution experiment performed on the neutron tomograph instrument (NeXT) located at Institut Laue-Langevin in Grenoble, France. The main goal of this experiment (PIN43) was to capture the flow field at various points during the evolution of a wormhole by way of contrast injections of light water (H_2O) into the sample saturated with heavy water (D_2O). As such, the pressure curve (Fig. 2) exhibits several pauses in which the contrast injection portion of the experiment was performed. As the sample must be saturated with heavy water, the acid used in this case was HCl dissolved in D_2O with a concentration of 0.1M. The flow rate in this experiment was set to 0.5mL/min, and the core was 58.7mm long. In this experiment 126 scans were taken with an acquisition time of 7 minutes 20 seconds and a voxel size of 43.5 micrometers.

The results of this experiment were consistent with that in the main text, with pressure drops associated with tip propagation speedups (Fig. 2), which in turn are spatially correlated to regions of large average grayscale intensities (permeability barriers; Fig. 3). Additionally, the sample exhibits two fractal dimensions (Fig. 4): one for lower length scales of 2.14 (for 43.5μm$\leq l \leq$ 1mm) and one for larger length scales of 2.72 (for 2mm $\leq l \leq$ 8.7mm) resulting from a bulk material interrupted by recrystallized groups of grains. The methods used for generating the per slice intensity average and ACF(l) computation are the same as in the main text; however, an additional processing step to remove

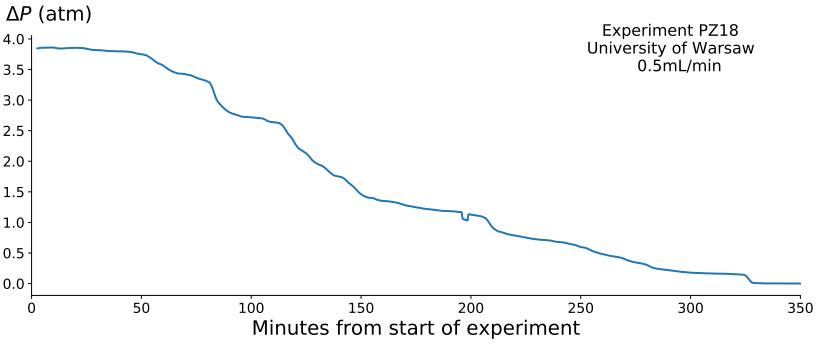

Figure 1: Pressure evolution log of an experiment designated PZ18 (18th experiment on Pińczów Limestone). Flow rate in this experiment was 0.5mL/min.

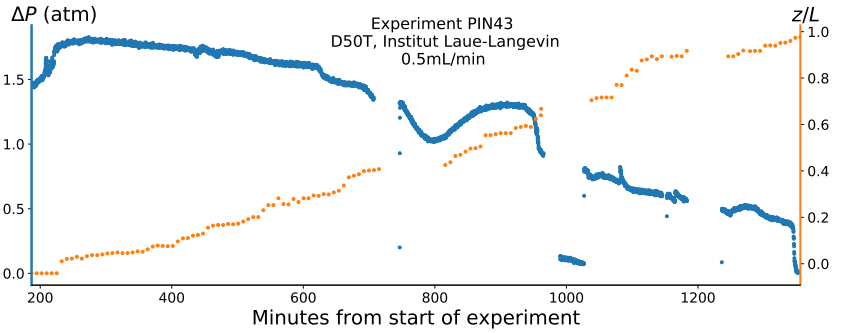

Figure 2: Pressure evolution log from experiment PIN43, along with tip position. This core was 58.7mm long, acidized with HCl dissolved in D_2O (0.1M) with a flow rate of 0.5mL/min. Acidization was paused several times during this experiment to capture the flow field with neutron tomography. Pressure rising to pre-pause levels after each pause is due to fluid density differences between D_2O/HCl and H_2O as remaining H_2O is flushed from the core.

a vertical (axially oriented) variation in beam intensity was performed prior. To remove the bias the average intensity of the core holder in the image is computed per slice by calibrating the intensity for each slice such that the same median intensity within the core holder region is maintained, i.e., each slice has the operation

$$g(\mathbf{r}) \cdot \text{median}(< g(\mathbf{r}) >_{\text{ch}(z)})_z / < g(\mathbf{r}) >_{\text{ch}(z)} \tag{1}$$

applied, where $\mathbf{r} = (x, y, z)$ are the position pixels, $< g(\mathbf{r}) >_{\text{ch}(z)}$ is the mean grayscale intensity within the core holder slice at a given z, and $\text{median}(\dots)_z$ is a median over z slices.

We also present additional data from the experiment in the main text, in the form of wormhole length (L_W over time (Fig. 5) compared to the z-extent of the wormhole and pressure over time, indicating lateral movement of the wormhole.

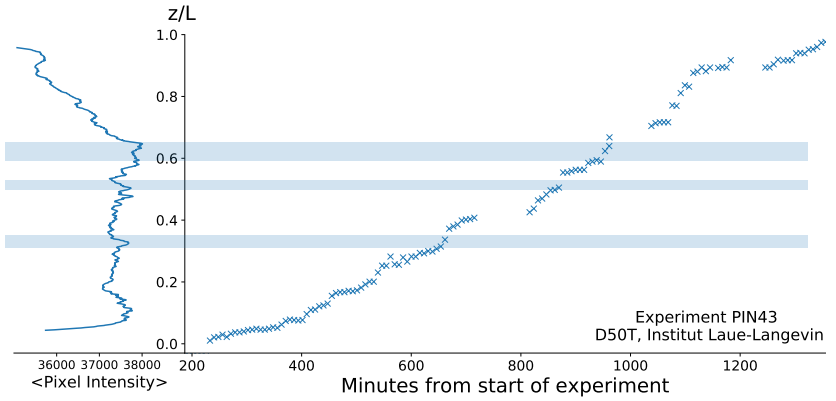

Figure 3: Tip position correlated to average pixel intensity of the core used in the PIN43 experiment. Tip speedups correlate spatially with the presence of peaks in the average intensity, corresponding to regions of high solid content (spar and recrystallized grains) within the core. The decreased pixel intensity at the ends of the sample is most likely a computed tomography artifact.

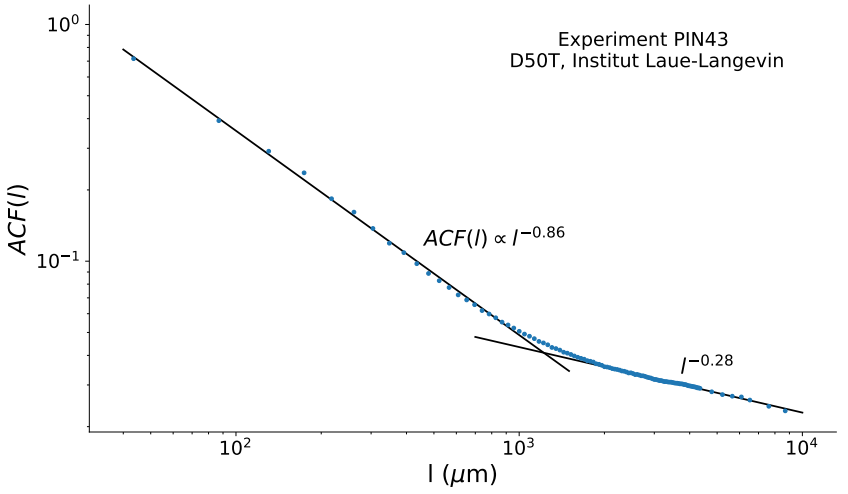

Figure 4: Autcorrelation function for the core used in the PIN43 experiment. This core exhibits the same switch over in fractal dimension as in the core in the main text, occurring at the 1mm scale.

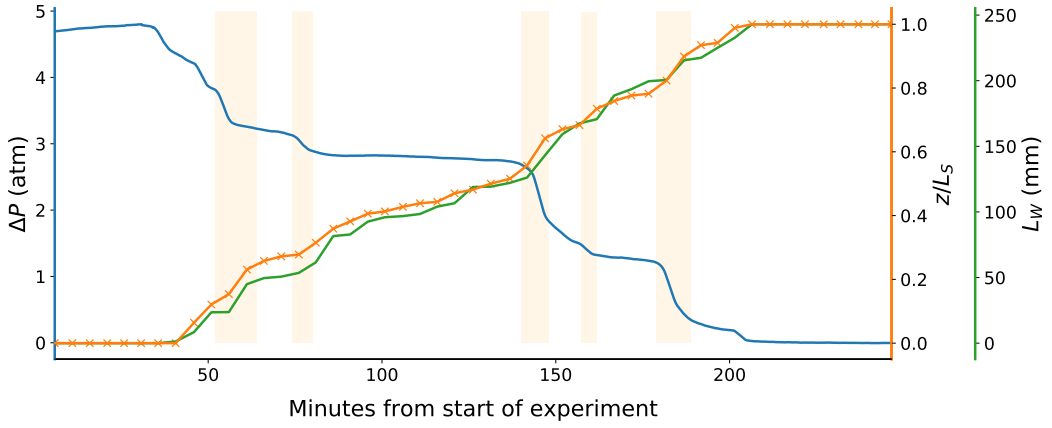

Figure 5: Wormhole length, L_W, over time compared to z-extent (z/L_S, where L_S is length of the sample) and pressure over time for the experiment presented in the main text. As the wormhole is tortuous and migrates laterally, L_W can be longer than the sample length (115mm).

2. Thin Section Data

Thin sections were taken along a 115mm long core at 10 (Fig. 6), 20 (Fig. 7), 30 (Fig. 8), 35 (Fig. 9), 50 (Fig. 10), 60 (Fig. 11), 70 (Fig. 12), and 80mm (Fig. 13). Autocorrelation data were computed for each thin section with l between 1 and 1500 (base 10 logarithmic spacing) pixel distance. Pixel distance is converted to micrometers by the pixel size of thin section imaging. For 10, 20, 30, and 35mm the pixel size is 1.7μm, while for 50, 60, 70, and 80mm the pixel size is 3.4μm.

For each thin section, either one or two linear regressions are performed on the data in log-log space (Figs. 5-12), depending if there is a transition to a different power law exponent (related to fractal dimension by $\mathrm{ACF}(l) \propto l^{-\alpha}$, $D_f = 3 - \alpha$). Transition of fractal dimension occurs at the scale of about 0.5mm, corresponding to the average grain size in the samples as determined by Figarska and Stańczak (Figarska-Warchoł and Stańczak, 2019). The average power law exponent for the whole rock thin section in the case of a single power law (at 10mm and 30mm), or the for lower range in the case of two power laws (20, 30, 35, 50, 60, 70mm) is 0.74, corresponding to a fractal dimension of 2.26. The average power law exponent at larger ranges is 0.41, for a fractal dimension of 2.59. These averaged numbers are close to the lower and upper fractal dimensions (2.2 and 2.55, respectively) derived from tomography of the pre-dissolved sample used in the experiment. The thin section at 80mm is an outlier, with a single fractal dimension of 2.59 for both scales, indicating a highly correlated structure similar to the upper ranges in the recrystallized regions; indeed, this thin section contains several large algal structures within it across both scales (Fig. 13). Power law exponents for each thin section and their corresponding fractal dimension are listed in Table 1.

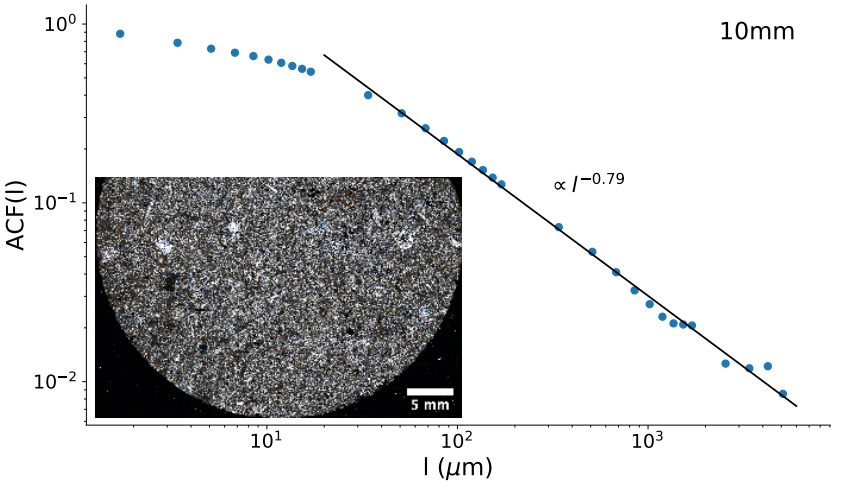

Figure 6: ACF(l) for thin section taken at 10mm from core face, exhibiting a single power law for all data with $34\mu m \leq l \leq 2550\mu m$.

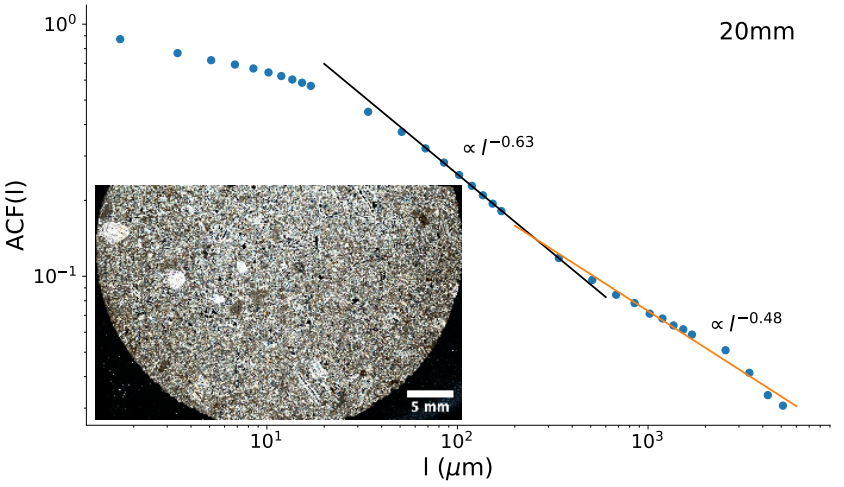

Figure 7: ACF(l) for thin section taken at 20mm from core face, exhibiting two power laws: one for data $34\mu m \leq l \leq 350\mu m$, and another for $510\mu m \leq l \leq 2550\mu m$.

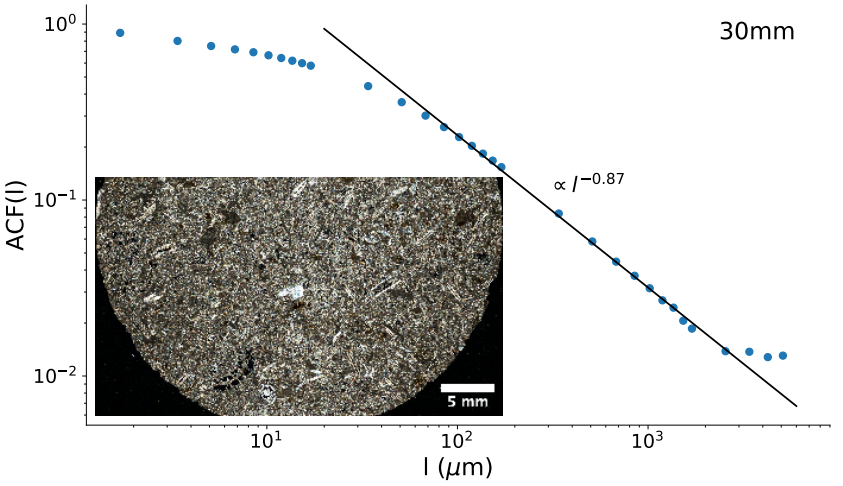

Figure 8: ACF(l) for thin section taken at 30mm from core face, exhibiting a single power law for data $34\mu m \leq l \leq 1530\mu m$.

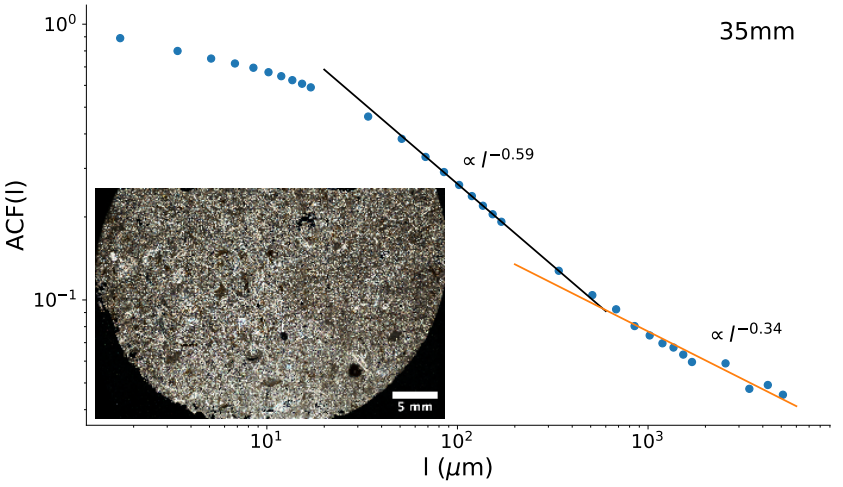

Figure 9: ACF(l) for thin section taken at 35mm from core face, exhibiting two power laws: one for data $34\mu m \leq l \leq 350\mu m$, and another for $510\mu m \leq l \leq 2550\mu m$.

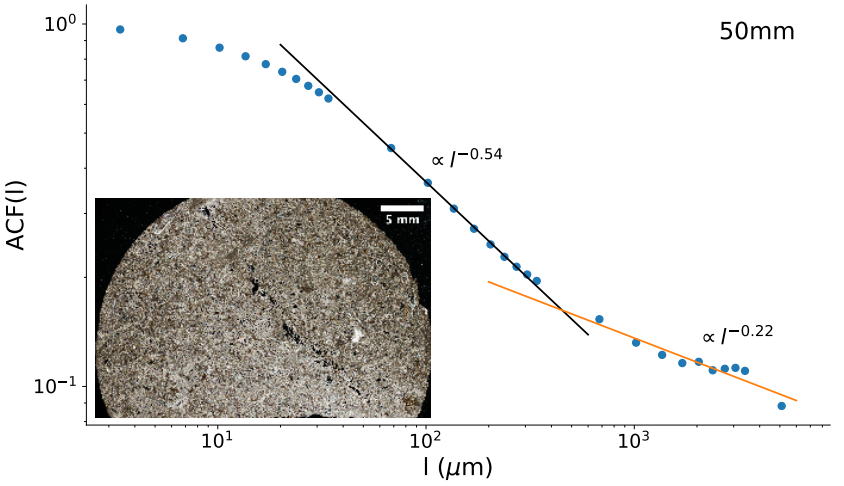

Figure 10: ACF(l) for thin section taken at 50mm from core face, exhibiting two power laws: one for data $68\mu m \leq l \leq 306\mu m$, and another for $680\mu m \leq l \leq 5100\mu m$.

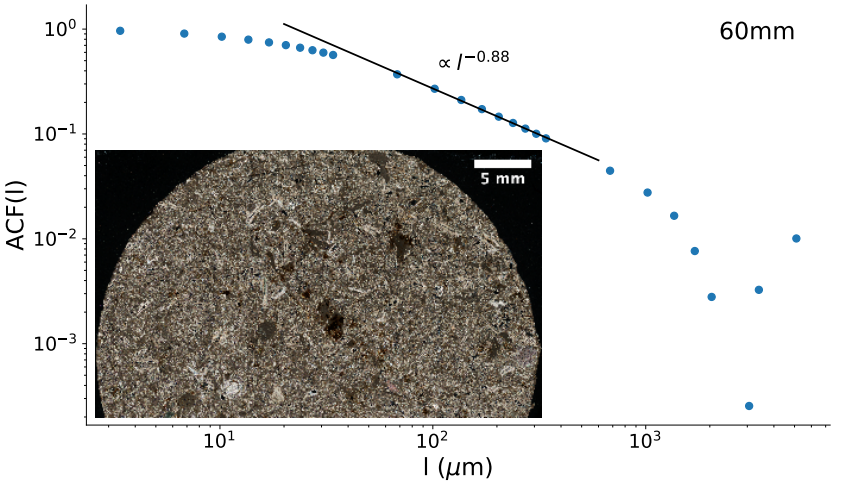

Figure 11: ACF(l) for thin section taken at 60mm from core face, exhibiting a single clear power law for the lower range of data $68\mu m \leq l \leq 340\mu m$.

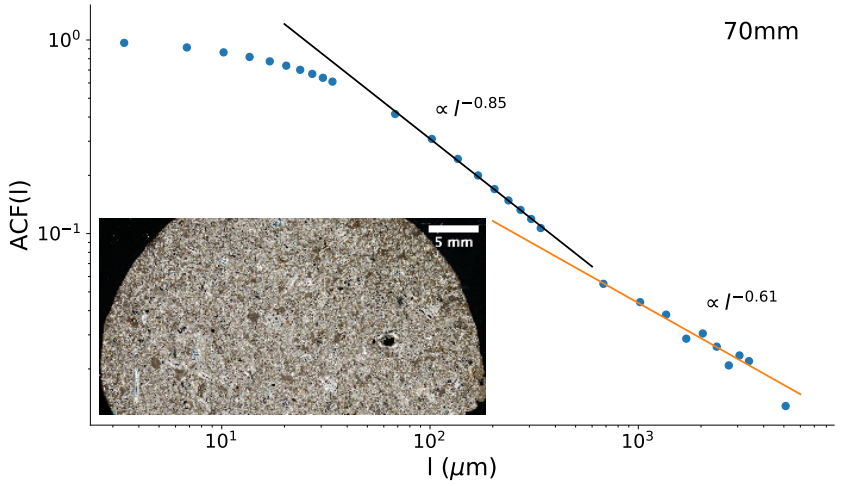

Figure 12: ACF(l) for thin section taken at 70mm from core face, exhibiting two power laws: one for data $68\mu m \leq l \leq 340\mu m$, and another for $680\mu m \leq l \leq 3400\mu m$.

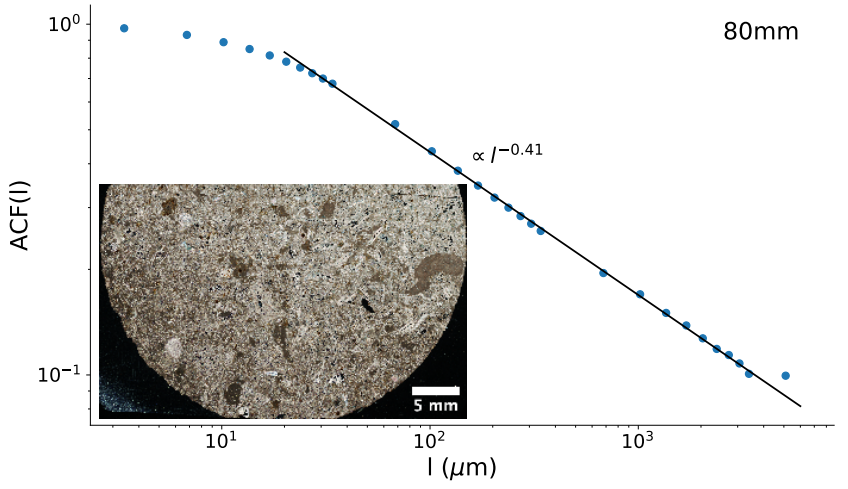

Figure 13: ACF(l) for thin section taken at 80mm from core face, exhibiting a single power law for all data with $68\mu m \leq l \leq 3500\mu m$.

Table 1
Power law fit exponents to autocorrelation data for each thin section, and corresponding fractal dimension.

Thin sections exhibiting a single fractal dimension				
Thin section	α		D_f	
10	0.79		2.21	
30	0.87		2.13	
80	0.41		2.59	
Thin sections exhibiting two fractal dimensions				
	Lower α	Upper α	Lower D_f	Upper D_f
20	0.63	0.48	2.37	2.52
35	0.59	0.35	2.41	2.65
50	0.54	0.22	2.46	2.78
60	0.88	-	2.12	-
70	0.85	0.61	2.15	2.39

3. Imaging Experiment

To determine optimal acquisition settings three static scans of a partially dissolved core were performed within the cell set up as in a dissolution experiment. The voxel resolutions used were 42, 84.5, and 169 micrometers. As the wormhole tip position is the same for each resolution (Fig. 14), 169 micrometer voxel resolution was chosen to minimize scanning time, despite the additional noise added that increases wormhole volume (Table 2). Binning of voxels for 169 micrometers also tightens the grayscale distribution (Fig. 15) and shifts the threshold for the wormhole and pores.

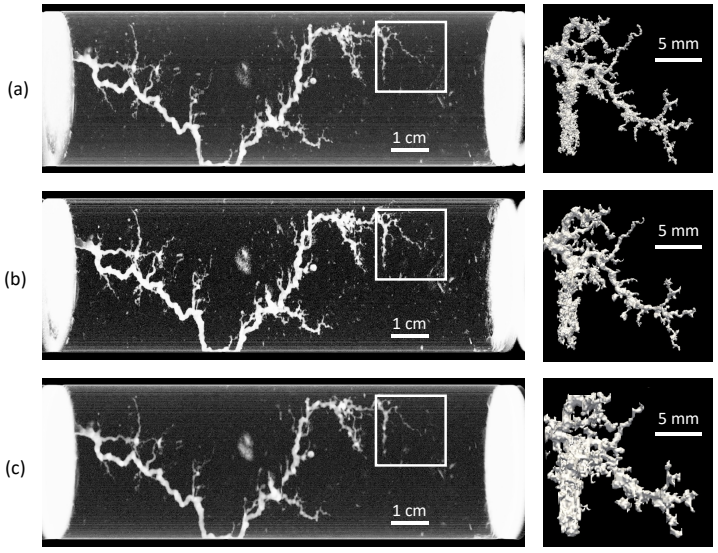

Figure 14: Projections of the entire wormhole in grayscale shades from tomography (left panels) and wormhole tip region extracted using connected components (flood fill) segmentation (right panels), for 42 micrometers (a), 84.5 micrometers (b), and 169 micrometers (c). The gross morphology of the wormhole is maintained at each resolution, though fine details are lost for larger voxel sizes (e.g., bulkier/merged branches). While finer details are smeared out, the main feature of interest, the ultimate wormhole tip position, is remains the same for the three resolutions.

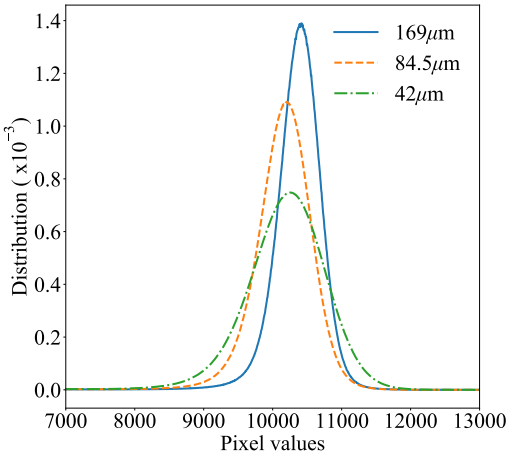

Figure 15: Grayscale distribution for 42, 84.5, and 169 micrometer voxel resolutions. Distributions are normalized so that the area under the distribution is unity for direct comparison.

Table 2
Thresholds and volumes at different resolutions.

Voxel size (μm)	Threshold	Volume (voxels)	Volume (mm^3)
42	8450	9012746	668
84.5	8450	1000227	603
169	9495	238432	1150

4. Wormhole Growth Videos

Experiment capturing the geometry of wormhole growth through X-Ray tomograpy, along with pressure required to drive fluid through the sample at a constant rate. Duration of each scan is 5 minutes. The rock type, Pińczów Limestone, shows a different type of pressure evolution behavior than typical limestones, which show a linear pressure change over time. Instead, Pińczów Limestone curves exhibit "plateaus" and "jumps". Despite seemingly little evolution in the plateaus, the wormhole does continue to grow, with a nearly constant velocity.

Two videos are supplied. In video S1, for visualization purposes, the wormholes are processed by the connected component algorithm (see A 3.2). While this is usually beneficial in terms of the image sharpness and clarity due to the removal of small pieces caused by the inherent image noise, a potential downside is that the pieces of the wormhole itself may be removed in the process. This can occur particularly around the tip, where the wormhole becomes thin and may appear discontinuous. Therefore, we also include another video (S2), in which the connected component algorithm has not been applied, and the extent of the wormhole can thus be identified with better precision.

References

Figarska-Warchoł, B. and Stańczak, G. (2019). The effect of petrographic characteristics on the physical and mechanical properties of currently exploited pińczów limestones–a type of leitha limestone (carpathian foredeep, southern poland). *Min. Resour. Manag.*, 35.